Gas infall and possible circumstellar rotation in R Leo*

J. P. Fonfría[1], M. Santander-García[2], J. Cernicharo[1], L. Velilla-Prieto[3], M. Agúndez[1], N. Marcelino[1], and G. Quintana-Lacaci[1]

[1] Molecular Astrophysics Group, Instituto de Física Fundamental, CSIC, C/ Serrano, 123, 28006, Madrid (Spain); e-mail: jpablo.fonfria@csic.es
[2] Observatorio Astronómico Nacional, OAN-IGN, Alfonso XII, 3, E-28014, Madrid (Spain)
[3] Dept. of Space, Earth, and Environment, Astronomy and Plasma Physics Division, Chalmers University of Technology, Onsala Space Observatory, S-439 92 Onsala (Sweden)

February 11, 2019

ABSTRACT

We present new interferometer molecular observations of R Leo taken at 1.2 mm with the Atacama Large Millimeter Array with an angular resolution up to $\simeq 0\rlap{.}''026$. These observations permitted us to resolve the innermost envelope of this star, which revealed a complex structure that involves extended continuum emission and molecular emission showing a non-radial gas velocity distribution. This molecular emission displays prominent red-shifted absorptions located immediately in front of the star, which are typical footprints of material infall. This emission also shows lateral gas motions compatible with a torus-like structure.

Key words. stars: AGB and post-AGB — stars: individual (R Leo) — circumstellar matter — stars: mass-loss — techniques: interferometric — techniques: high angular resolution

1. Introduction

R Leo is an O-rich asymptotic giant branch star (AGB) located at $\simeq 70-85$ pc from Earth (De Beck et al. 2010; Ramstedt & Olofsson 2014). It has an effective temperature of $\simeq 2500-3000$ K and an angular diameter of $\simeq 0\rlap{.}''025 - 0\rlap{.}''030$ in the K band (Perrin et al. 1999; Fedele et al. 2005; Wittkowski et al. 2016). It pulsates with a period of $\simeq 310$ days, ejecting processed material with a low mass-loss rate of $\simeq 1.0 \times 10^{-7}$ M$_\odot$ yr^{-1} and a terminal velocity of $6 - 9$ km s^{-1} (Bujarrabal et al. 1994; Cernicharo et al. 1997).

The continuum at different wavelengths (optical, infrared, and millimeter) together with the thermal and maser molecular emissions coming from this star have been analysed with different observing techniques (e.g. Castelaz & Luttermoser 1997; Pardo et al. 1998; Ryde et al. 1999; González-Delgado et al. 2003; Soria-Ruiz et al. 2007). Some of these observations suggested the existence of complex structures in the innermost envelope. Cernicharo et al. (1994) carried out lunar occultation observations of the SiO($v = 1, J = 2 - 1$) maser, finding a low-velocity structure within the $0\rlap{.}''5$ sized region around the star that could be interpreted as a developing bipolar outflow or a rotating torus. However, the limited spatial information perpendicular to the occultation direction achieved was insufficient to properly constrain this structure. Additional asymmetries were found at larger scales by Plez & Lambert (1994), suggesting that the structure revealed by Cernicharo et al. (1994) could be part of a larger structure that covers a significant fraction of the envelope.

In this Letter, we present new interferometer observations of CO and ^{29}SiO towards the AGB star R Leo. They were carried out with the Atacama Large Millimeter Array (ALMA) with an angular resolution of up to $0\rlap{.}''026$, which is comparable to the size of the star.

2. Observations

We observed R Leo with ALMA during Cycles 4 and 5 within the frame of project 2016.1.01202.S. Array configurations C40-2, C40-5, C40-6, and C43-9 were used and provided baselines from 15 m up to 13.9 km. These observations give a complete view of the envelope of R Leo at different scales along $\simeq 1.25$ pulsation periods. The observation details can be found in Table 1.

Four spectral windows covered the frequency ranges $212.7 - 216.8$ and $227.5 - 231.5$ GHz with a channel width of 488 kHz. The flux, bandpass, and pointing were calibrated in the usual way by observing J0854+2006 or J1058+0133. We estimate a flux error $\simeq 5\%$. The phase calibrators and check sources J1002+1216, J1008+0621, and J0946+1017 were periodically observed. R Leo was observed twice with configuration C43-9. In the first run (run A), the baseline of one spectral window was affected by strong spurious periodic spikes, the weather was not good enough for this demanding configuration (PWV $\simeq$ 1.2 mm), and the uv plane coverage was limited. The data quality greatly increased during the second run (run B), and run A was deprecated. The data were calibrated with the pipeline in CASA 4.7.2 (McMullin et al. 2007).

Table 1. Observation summary

Conf./Run	Date	Phase	PSF HPBW ("×")	P.A. (deg)	W	MRS (")	Continuum Peak (mJy beam⁻¹)	Integral (mJy)	Gaussian Fit Peak (mJy beam⁻¹)	D. FWHM ("×")	D. P.A. (deg)
C40-2	2017-Mar-22	0.80	1.560 × 1.080[a]	80	N	11.6	91.16 ± 0.12	105.8 ± 0.6	—	—	—
C40-5	2017-May-03	0.94	0.387 × 0.359[b]	45	N	4.5	91.10 ± 0.16	111.6 ± 1.1	—	—	—
C40-6	2016-Oct-01	0.25	0.186 × 0.157[c]	32	N	1.6	101.0 ± 0.3	140.2 ± 2.1	—	—	—
C43-9/A	2017-Sep-21	0.40	0.096 × 0.035[d]	45	N	0.4	68.19 ± 0.20	103.1 ± 1.6	—	—	—
			0.071 × 0.025[e]	32	U		52.55 ± 0.18	103.3 ± 1.8	—	—	—
C43-9/B	2017-Oct-27	0.50	0.060 × 0.046[f]	134	N	0.6	45.10 ± 0.21	90 ± 3	37.8	0.042 × 0.034	173
									7.7	0.190 × 0.021	50
			0.026 × 0.026[g]	—	U		21.38 ± 0.16	85 ± 3	16.5	0.045 × 0.030	155
									5.4	0.132 × 0.022	50

Notes. From left to right, the columns contain the ALMA configuration and the run for duplicated observations, the observation date, the optical pulsation phase (pulsation period = 310 days; JD_{max} = 2457896 following AAVSO[a]), the size and P.A. of the synthesised PSF, the visibility weighting (N, "natural", means robust = 1 and U, "uniform", robust = 0.1 in GILDAS), the maximum recoverable scale, the continuum peak for every configuration, the continuum integral above the 5σ level contours, the peak emission of the Gaussian components of the fit, and the FWHM and P.A. after deconvolution. When the Gaussian fit is not provided (—), the source can be considered as point-like. The errors of the continuum peak and the continuum integral do not consider the flux calibration uncertainties. The statistical errors of the Gaussian fit are always $\lesssim 5\%$. (a-g) The characteristic HPBWs, θ_{PSF}, are 1″.30, 0″.37, 0″.17, 0″.058, 0″.042, 0″.052, and 0″.026, respectively.

[a] https://www.aavso.org/

Mapping and data analysis were almost fully performed with GILDAS[1]. The images were restored adopting a robust parameter of 1.0 and 0.1 (natural and uniform weighting, hereafter). We estimate a positional uncertainty for the highest angular resolution of $\simeq$ 0″.005 from the standard deviation of the emission peak position of the phase calibrator over time (Menten et al. 2006; Fonfría et al. 2014).

In this Letter, we focus on the short-scale observations to describe the stellar vicinity. The analysis of the envelope through the larger-scale maps is beyond the scope of this work and will be presented elsewhere (Fonfría et al., *in preparation*). Owing to the stellar pulsation phase incoherence and the long time lag ($\simeq$ 1.1 yr), the data taken with the C40-6 and C43-9 configurations were not merged to prevent artefacts.

3. Results and discussion

3.1. Structure of the continuum emission

The observations show one continuum emission source in the region of the sky that is covered by the primary beam (Fig. 1). It peaks at $(RA, DEC) = (09^h47^m33^s.4915 \pm 0^s.0004, 11°25'42''.899 \pm 0''.005)$.

The highest resolution observations show a compact source surrounded by a faint extended brightness distribution elongated roughly along the northeast-southwest direction (Fig. 1). It is noteworthy that the maximum recoverable scale (MRS; $\simeq$ 0″.6) is similar to the size of the extended emission in Fig. 1, which is $\simeq$ 0″.35 above the 5σ level. Thus, the array could be filtering emission, which would prevent us from deriving reliable brightness temperatures for the star.

The continuum emission can be described by two Gaussian-like components: one compact and one extended component (Table 1). We can estimate the size of the continuum source at 7 mm at the same pulsation phase as during our observations ($\simeq$ 0.50) from the results reported by Matthews et al. (2018) assuming first a uniform disc fit, using linear interpolations, and finally scaling the result to obtain a Gaussian size. The result is

[1] https://www.iram.fr/IRAMFR/GILDAS
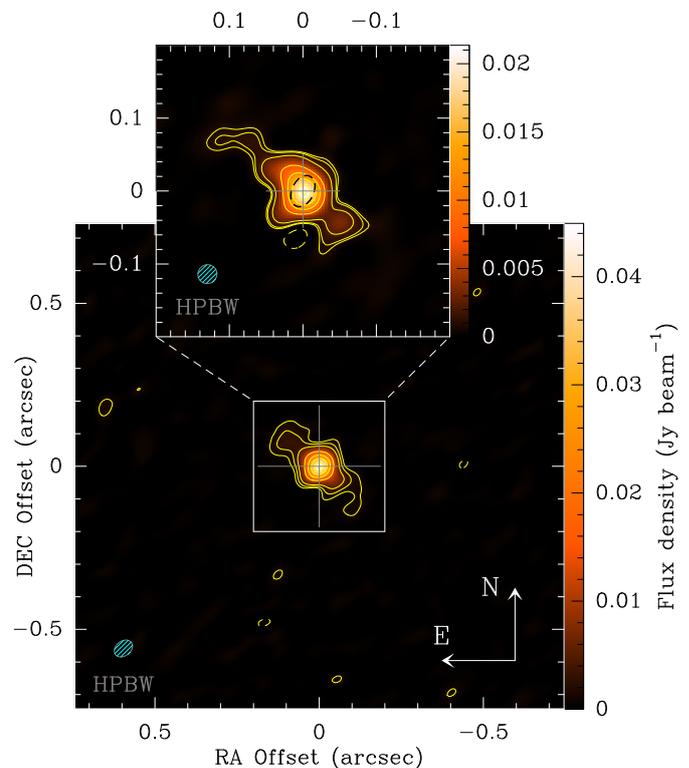
Fig. 1. Continuum emission observed with configuration C43-9, run B, assuming natural weighting (*lower*; $\theta_{PSF} \simeq$ 0″.052) and uniform weighting (*upper*; $\theta_{PSF} \simeq$ 0″.026). The lowest contours are at $\pm 5\sigma$ (2.3% and 3.75% of the maximum for the lower and upper insets). The rest are at 5, 10, 30, 50, 70, and 90% of the maximum. The grey crosses indicate where the emission peaks in the uniformly weighted map. The star is plotted in the upper inset as a dashed ellipse. Its size is the deconvolved size of the compact emission component.

$\simeq$ (0″.035 ± 0″.006)×(0″.025 ± 0″.003), smaller than the size of our compact source (0″.045×0″.030). This can only occur if the star is surrounded by a continuum source that emits more at 1 mm than at 7 mm, like a dusty shell (Norris et al. 2012). All this is com-

patible with the extended continuum component (size $\simeq 0.''05$) found by Paladini et al. (2017) in the mid-IR around the star. For simplicity, we here consider this compact component as the star.

The extended Gaussian-like component is elongated along the northeast-southwest direction. Its deconvolved size is smaller than the angular resolution provided by the C40-6 configuration ($\theta_{PSF} \simeq 0.''17$) and it is not evident in the corresponding map. The ellipticity of this component is $e = 1 - \theta_{min}/\theta_{maj} \simeq 0.83$, where θ_{maj} and θ_{min} are the deconvolved major and minor axes (Table 1). Because no extended emission has been discovered at longer wavelengths (Reid & Menten 2007; Matthews et al. 2018), the extended component would be produced by dust.

3.2. Complex molecular line profiles in the vicinity of the star

The CO and ^{29}SiO lines at the central pixel reveal profiles with emission and absorption components, suggesting the presence of a complex structure (Fig. 2). The CO($v = 0, J = 2 - 1$) and ^{29}SiO($v = 0, J = 5 - 4$) lines observed with an angular resolution $\theta_{PSF} \simeq 0.''17$ (Table 1) comprise a main emission contribution roughly centred at a systemic velocity of -0.5 km s^{-1} (Teyssier et al. 2006) and a prominent red-shifted absorption of $\simeq 25\%$ of the continuum that peaks at $\simeq 8$ km s^{-1}. The ^{29}SiO line observed with $\theta_{PSF} \simeq 0.''052$ is dominated by a strong absorption peak at $\simeq -2.5$ km s^{-1} ($\simeq 70\%$ of the continuum), while the CO line shows a clear inverse P-Cygni profile. Line CO($v = 1, J = 2 - 1$) also shows a similar profile, and its absorption component peaks at $\simeq 10$ km s^{-1}. The ^{29}SiO($v = 1, J = 5 - 4$) line lacks emission but shows a broad absorption that peaks at $\simeq 3 - 6$ km s^{-1}. All these absorptions extend up to velocities $\simeq 10 - 15$ km s^{-1}, higher than the terminal expansion velocity ($\simeq 6 - 9$ km s^{-1}; Bujarrabal et al. 1994; Cernicharo et al. 1997; De Beck et al. 2010; Ramstedt & Olofsson 2014). No absorption is observed for all these lines with $\theta_{PSF} \simeq 0.''37$ and $1.''30$, except for ^{29}SiO($v = 1, J = 5 - 4$). This line displays blue- and red-shifted absorptions and a well-differentiated, narrow emission component at the systemic velocity. The large variations seen between the $v = 1$ lines, which are expected to arise very close to the star and are observed with $\theta_{PSF} \simeq 0.''17$ and $0.''052$, indicate substantial excitation changes throughout a single pulsation period.

All this suggests that (1) gas is moving away from us in front of the star, which produces the red-shifted absorptions, (2) most of the emission comes from directions that do not enclose the star, and (3) the upper level involved in the ^{29}SiO($v = 1, J = 5 - 4$) line might be strongly drained, considering that this line forms in shells with temperatures $\gtrsim 1500$ K, where the ^{29}SiO($v = 0, J = 5 - 4$) do show a noticeable emission. This effect could invert the populations of the levels involved in the ^{29}SiO($v = 1, J = 6 - 5$) line, which might show maser emission (Cernicharo et al. 1991; González-Alfonso & Cernicharo 1997).

3.3. Gas infall and indications of rotation

The CO and ^{29}SiO emission distributions seen in the vicinity of the star are shown in Fig. 3. The integrated emission of line ^{29}SiO($v = 0, J = 5 - 4$) mapped with $\theta_{PSF} \simeq 0.''17$ (Fig. 3, upper left panel) shows a bipolar structure which extends roughly along the east-west direction (P.A. $\simeq 100°$). Lower level contours ($\simeq 30 - 50\%$ of the peak emission) are elongated along the perpendicular direction. The east-west structure can be separated into different contributions in the velocity range $[-15, 7.6]$ km s^{-1}: (1) a blue-shifted contribution centred
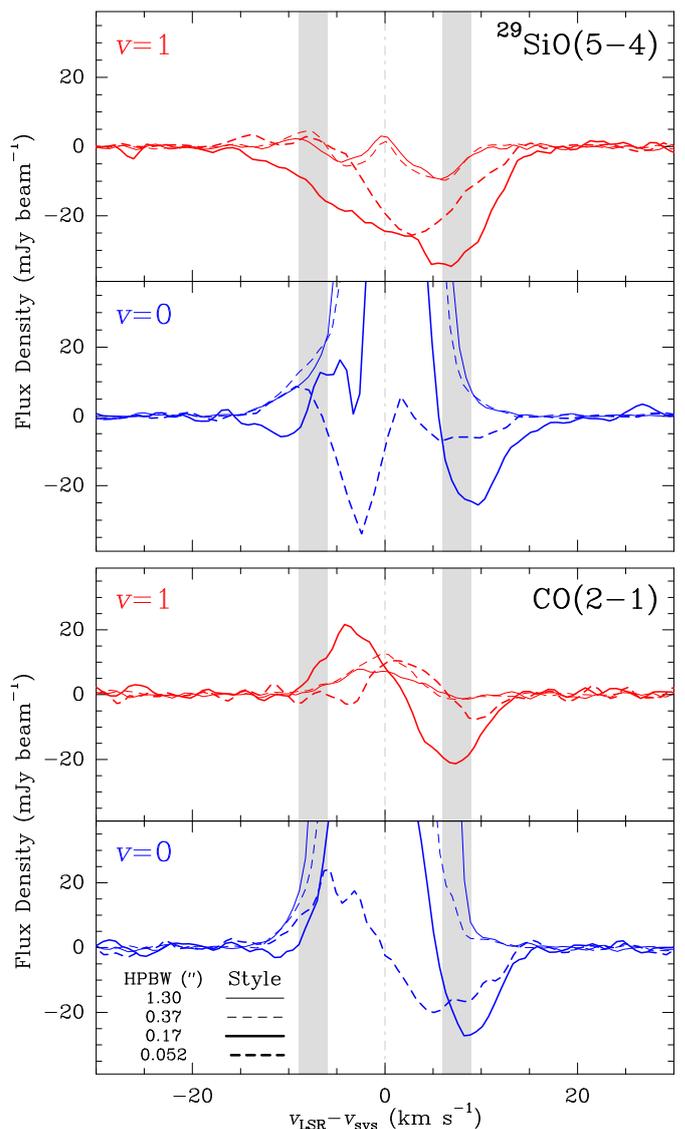
Fig. 2. Spectra in the central pixel of the CO($2-1$) and ^{29}SiO($5-4$) lines ($v = 0$ in blue and $v = 1$ in red) acquired with different ALMA configurations. The number of pixels in the PSF is the same for every configuration. The grey vertical bands indicate the gas expansion velocity derived from single-dish observations. We have assumed a $v_{sys} = -0.5$ km s^{-1} (Teyssier et al. 2006).

at $\simeq 0.''1$ to the east of the star, (2) a red-shifted contribution centred at $\simeq 0.''2$ to the west, and (3) another contribution at the systemic velocity covering the same region of the envelope as the previous ones. In the middle of the red- and blue-shifted contributions is an absorption in the velocity range $[7.6, 15]$ km s^{-1}, also seen in the ^{29}SiO($v = 1, J = 5 - 4$) line, which matches the star within the positional uncertainty.

The division of the CO($v = 0, J = 2 - 1$) line into velocity intervals reveals a more complex structure (Fig. 3, upper right panel). The emission at the systemic and positive velocities of the $v = 0$ and 1 lines comes from the western hemisphere of the envelope. The red-shifted absorption of the $v = 0$ line matches the star but it is slightly shifted towards the southwest for the $v = 1$ line. The blue-shifted emission of the $v = 1$ line is mostly absent. The blue- and red-shifted emissions of the $v = 0$ line and the emission of the $v = 1$ line overlap to the south. There is a CO emission deficit at velocities $\gtrsim 3$ km s^{-1} due northeast.
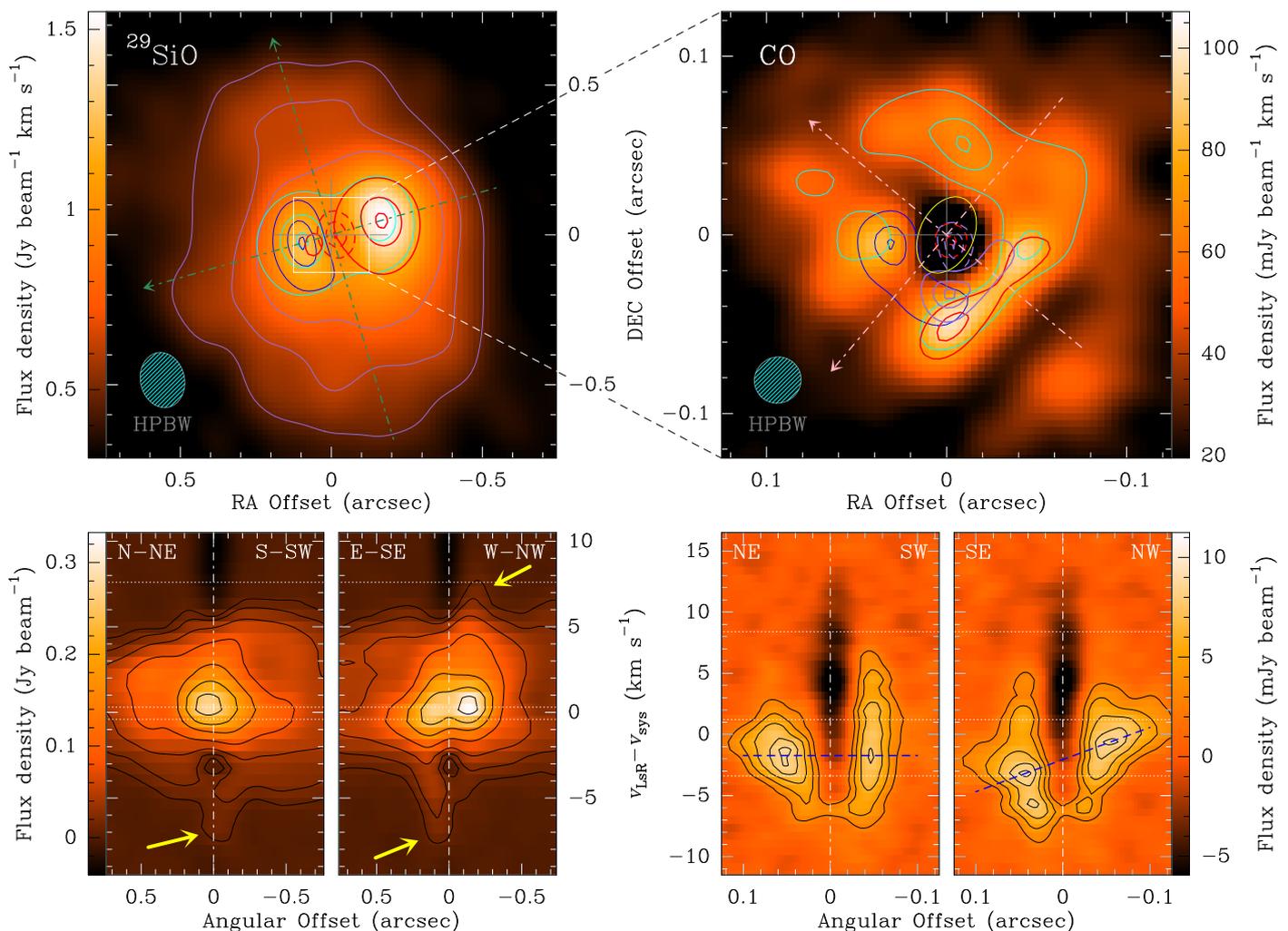
Fig. 3. ^{29}SiO and CO emission in the sub-arcsec region. (*Upper left*) ^{29}SiO($v = 0, J = 5 - 4$) line ($\theta_{PSF} \simeq 0\rlap{.}''17$). The purple contours are at levels 30, 40, and 50% of the integrated emission peak. The green dash-dotted arrows describe the main directions of the total emission. The solid blue, red, and cyan contours are the blue-shifted, red-shifted, and systemic velocity emissions ([$-15, -0.4$], [$0.3, 7.6$], and [$-0.4, 0.3$] km s^{-1}). The dashed red contours describe the red-shifted absorption ([$7.6, 15$] km s^{-1}), which spatially matches the absorption of the $v = 1$ line. (*Upper right*) CO($v = 0, J = 2 - 1$) line ($\theta_{PSF} \simeq 0\rlap{.}''026$). The solid blue and red contours are the blue- and red-shifted emission ([$-15, -3.4$] and [$1.2, 8.4$] km s^{-1}). The cyan contours are the emission around the systemic velocity ([$-3.4, 1.2$] km s^{-1}; $v_{sys} = -0.5$ km s^{-1}). The dashed red contours are the red-shifted absorption. The solid and dashed purple contours are the emission and absorption of the CO($v = 1, J = 2 - 1$) line ([$-3.3, 6.9$] and [$6.9, 15$] km s^{-1}). The thin yellow ellipse represents the star and the dash-dotted pink arrows define the main directions of the continuum emission. In both insets, the contours are at levels 70, 90, and 99% of the peak emission/absorption. The grey crosses position the continuum emission peak. (*Lower left* and *right*) Position-velocity diagrams of the ^{29}SiO($v = 0, J = 5 - 4$) and CO($v = 0, J = 2 - 1$) lines (*left* and *right*, respectively) along the corresponding main directions. The horizontal dotted lines are the limits between the previous velocity ranges. The yellow arrows (*left*) point out features in the diagrams typical of the emission of rotating gas. The blue dashed lines (*right*) connect the peak emissions along the northeast-southwest and southeast-northwest, revealing the dependence of the Doppler shift on the direction. The contours are at 3, 7, 15, 30, 50, 70, and 90% (^{29}SiO; $9.5\sigma \simeq 3\%$) and 30, 50, 70, 87, and 97% (CO; $5\sigma \simeq 3.6\%$) of the peak emissions.

The whole picture seems to be roughly symmetric around the northeast-southwest direction. This main direction is compatible with that defined by the CO($v = 0, J = 2 - 1$) emission mapped with lower spatial resolutions (Fonfría et al, *in preparation*) and by the continuum-extended emission (Fig. 1). The position-velocity diagram along the southeast-northwest direction (Fig. 3, lower right panel) is similar to the diagrams of the rotating discs in expansion that have been found in several post-AGB stars, except for the infalling gas (Bujarrabal et al. 2016, 2017).

The disagreement between the symmetry axes in the ^{29}SiO and CO maps could be consequence of an inhomogeneous chemistry favoured by anisotropic physical and chemical conditions. Excitation effects cannot be ruled out considering the many

blended lines shown by SiO and its isotopologues that display maser emission in this and other O-rich stars (e.g. González-Alfonso & Cernicharo 1997; Pardo et al. 1998).

Two models can explain the observations reasonably well. We describe them below.

1. Gas rotating around the axis described by the extended continuum emission (northeast-southwest direction; P.A. $\simeq 50°$). Part of the gas responsible of the blue-shifted emission to the southeast would leave the main stream during its spinning movement towards the northwest as a result of instabilities or interactions with the recently ejected matter, falling onto the star with a Doppler velocity relative to the systemic velocity up to $\simeq 10 - 15$ km s^{-1} (Fig. 3, lower insets). The rest of the gas would continue to revolve around the star at an

average velocity of $\simeq 6-8$ km s^{-1}. A similar Doppler shift is expected for gas orbiting a star with a mass of $\simeq 0.5-1.0\ M_\odot$ if an orbital inclination of $\simeq 25° - 50°$ is assumed.

2. The previous rotating structure would exist as well, but there would not be any leakage resulting in gas falling onto the star. The red-shifted absorptions would be produced by radial movements of photospheric layers (or convective cells) through the stellar pulsation (Hinkle 1978; Hinkle & Barnes 1979a,b).

Contrary to what Vlemmings et al. (2017) claimed occurs in the photosphere of W Hya, where a bright spot has been suggested to be caused by the collision of infalling matter onto the star, we do not find any footprint of this phenomenon in our continuum maps. However, the angular resolution of our observations is insufficient to explore the stellar photosphere, and a similar bright spot could be highly diluted. Tatebe et al. (2008) found evidence of a hot spot in the southern part of R Leo that might have a counterpart in the millimeter range.

It can be argued that the Doppler velocities seen in our observations are related to random gas movements in the stellar photosphere or to effects of periodic shocks. Several works based on VLBI observations of SiO masers have been published for a number of AGB stars such as R Leo or TX Cam (e.g. Cotton et al. 2004; Soria-Ruiz et al. 2007; Gonidakis et al. 2013). The maser spots are assumed to live long enough to trace the gas movement very close the photosphere if a good sampling is adopted. Those observations are constrained to the shell where the maser emission is higher, which covers the region ranging from 0.″030 to 0.″040. They thus sample a region of the envelope that is considerably closer to the star than the region traced by our data. Common conclusions are therefore difficult to draw. In contrast to VLBI observations, the angular resolution of our observations is insufficient to describe random gas movements, which are cancelled out during the averaging performed by the PSF and contribute to broaden line widths.

A set of several clumps ejected with significant axial velocities resulting from ballistic trajectories, for instance, could also be suggested to comprise the detected structure. However, our observations show a highly continuous velocity field around the star that is difficult to explain assuming randomly ejected, discrete clumps with unconnected kinematical properties. Additionally, evidence exists of a rotating molecular torus in the envelopes of other AGB stars such as L2 Pup or R Dor (Kervella et al. 2016; Homan et al. 2018). This suggests that these structures might be more common than initially expected.

The existence of rotating gas in the surroundings of the star needs an angular momentum input because the rotation of an AGB star is expected to be very low. This extra angular momentum could be provided by a dipolar magnetic field (Matt et al. 2000) or an additional body (Vlemmings et al. 2018). The first scenario would require a plasma or a gas of charged particles to be coupled with the magnetic field. No continuum emission typical of a plasma has been detected, but dust grains are probably charged in the innermost envelope. A dipolar magnetic field could force the radially ejected grains to drag the gas, which would induce circumstellar rotation. Regarding the second scenario, no companion has been found in the optical and near-IR spectral ranges (Gatewood 1992), but this disagreement could be solved if it is a small, cold body such as a low-mass star or a Jovian planet instead. This idea has been invoked by Wiesemeyer (2009b) to explain the polarisation fluctuations detected in the SiO maser emission (Wiesemeyer et al. 2009a), which are also formed very close to the stellar photosphere. The existence of a planet orbiting an AGB star has also been suggested to be possible by Kervella et al. (2016), who claimed to have discovered what could be one of them in L2 Pup.

4. Summary and conclusions

We presented new interferometer observations of the AGB star R Leo. They were carried out with ALMA with a maximum angular resolution of $\simeq 0.″026$ and a MRS $\simeq 0.″6$.

The continuum emission can be described as a compact source surrounded by a highly collimated extended emission in the northeast-southwest direction. The CO maps show a 0.″1 sized rotating torus-like structure with its axis lying along the northeast-southwest direction. This structure could be explained by (1) either the action of a dipolar magnetic field on the radially expanding wind or (2) the presence of a small, cold companion (maybe a Jovian planet) that orbits the central star and injects angular momentum to the gas. This seemingly rotating structure is accompanied by evident red-shifted absorptions that could be produced by infalling gas coming from it or by the regular movement of the pulsating photosphere. At larger scales, ^{29}SiO also shows a torus-like structure with its axis roughly oriented along the north-south direction, which is not detected in the corresponding CO map. Its origin is unclear, but it may be produced by anisotropic physical and chemical conditions or unexpected excitation effects.

These observations reveal a highly complex structure in the envelope of R Leo that is tightly related to the changes undergone by this AGB star. They will be addressed accurately in the near future through detailed analyses of these and new larger-scale data.

References

Bujarrabal V., Fuente A. & Omont A., 1994, A&A, 285, 247
Bujarrabal V., Castro-Carrizo A., Alcolea J., et al., 2016, A&A, 593, A92
Bujarrabal V., Castro-Carrizo A., Alcolea J., et al., 2017, A&A, 597, L5
Castelaz M. W. & Luttermoser D. G., 1997, AJ, 114, 1584
Cernicharo J., Bujarrabal V. & Lucas R., 1991, A&A, 249, L27
Cernicharo J., Brunswig W., Paubert G. & Liechti S., 1994, ApJ, 423, L143
Cernicharo J., Alcolea J., Baudry A. & González-Alfonso E., 1997, A&A, 319, 607
Cotton W. D., Mennesson B., Diamong P. J., et al., 2004, A&A, 414, 275
De Beck E., Decin L., de Koter A., et al., 2010, A&A, 523, 18
Fedele D., Wittowski M., Paresce F., et al., 2005, A&A, 431, 1019
Fonfría J. P., Fernández-López M., Agúndez M., et al., 2014, MNRAS, 445, 3289
Gatewood G., 1992, PASP, 104, 23
González-Alfonso E. & Cernicharo J., 1997, A&A, 322, 938
González-Delgado D., Olofsson H., Kerschbaum F., et al., 2003, A&A, 411, 123
Gonidakis I., Diamond P. J. & Kemball A. J., 2013, MNRAS, 433, 3133
Hinkle K. H., 1978, ApJ, 220, 210
Hinkle K. H. & Barnes T. G., 1979a, ApJ, 227, 923
Hinkle K. H. & Barnes T. G., 1979b, ApJ, 234, 548
Homan W., Danilovich T., Decin L., et al., 2018, A&A, 614, 113
Kervella P., Homan W., Richards A. M. S., et al., 2016, A&A, 596, A92
Matt S., Balick B., Winglee R. & Goodson A., 2000, ApJ, 545, 965
Matthews L. D., Reid M. J., Menten K. M., & Akiyama K., 2018, AJ, 156 15
McMullin J. P., Waters B., Schiebel D., Young W., & Golap K. 2007, Astronomical Data Analysis Software and Systems XVI (ASP Conf. Ser. 376), ed. R. A. Shaw, F. Hill, & D. J. Bell (San Francisco, CA: ASP), 127
Menten K. M., Reid M. J., Krügel E., Claussen M. J., & Sahai R., 2006, A&A, 453, 301

Norris B. R. M., Tuthill P. G., Ireland M. J., et al., 2012, Nature, 484, 220
Paladini C., Klotz D., Sacuto S., et al., 2017, A&A, 600, A136
Pardo J. R., Cernicharo J., González-Alfonso E. & Bujarrabal V., 1998, A&A, 329, 219
Perrin G., Coudé du Foresto V., Ridgway S. T., et al., 1999, A&A, 345, 221
Plez B. & Lambert D. L., 1994, ApJ, 425, L101
Ramstedt S. & Olofsson H., 2014, A&A, 566, 145
Reid M. J. & Menten K. M., 2007, ApJ, 671, 2068
Ryde N., Gustafsson B., Hinkle K. H., et al., 1999, A&A, 347, L35
Soria-Ruiz R., Alcolea J., Colomer F., Bujarrabal V. & Desmurs J.-F., 2007, A&A, 468, L1
Tatebe K., Wishnow E. H., Ryan C. S., et al., 2008, ApJ, 689, 1289
Teyssier D., Hernández R., Bujarrabal V., Yoshida H. & Phillips T. G., 2006, A&A, 450, 167
Vlemmings W. H. T., Khouri T., O'Gorman E., et al., 2017, Nature Astron., 1, 848
Vlemmings W. H. T., Khouri T., De Beck E., et al., 2018, A&A, 613, L4
Weiner J., Hale D. D. S. & Townes C. H., 2003, ApJ, 589, 976
Wiesemeyer H., Thum C., Baudry A. & Herpin F., 2009a, A&A, 498, 801
Wiesemeyer H., 2009b, A&A, 501, 647
Wittkowski M., Chiavassa A., Freytag B., et al., 2016, A&A, 587, A12